Ion-Specific Control of the Self-Assembly Dynamics of a Nanostructured Protein Lattice

Behzad Rad,[†] Thomas K. Haxton,[†] Albert Shon,[†,⊥] Seong-Ho Shin,[†,§] Stephen Whitelam,[†] and Caroline M. Ajo-Franklin*,[†,‡]

[†]Materials Sciences Division, [‡]Physical Biosciences Division, and Synthetic Biology Institute, Lawrence Berkeley National Laboratory, Berkeley, California 94720-8075, United States, [§]Department of Chemistry, UC Berkeley, Berkeley, California 94720-1460, United States, and [⊥]Department of Chemical and Biomolecular Engineering, UC Berkeley, Berkeley, California 94720-1462, United States

ABSTRACT Self-assembling proteins offer a potential means of creating nanostructures with complex structure and function. However, using self-assembly to create nanostructures with long-range order whose size is tunable is challenging, because the kinetics and thermodynamics of protein interactions depend sensitively on solution conditions. Here we systematically investigate the impact of varying solution conditions on the self-assembly of SbpA, a surface-layer protein from *Lysinibacillus sphaericus* that forms two-dimensional nanosheets. Using high-throughput light scattering measurements, we mapped out diagrams that reveal the relative yield of self-assembly of nanosheets over a wide range of concentrations of SbpA and Ca^{2+}. These diagrams revealed a localized region of optimum yield of nanosheets at intermediate Ca^{2+} concentration. Replacement of Mg^{2+} or Ba^{2+} for Ca^{2+} indicates that Ca^{2+} acts both as a specific ion that is required to induce self-assembly and as a general divalent cation. In addition, we use competitive titration experiments to find that 5 Ca^{2+} bind to SbpA with an affinity of $67.1 \pm 0.3\ \mu$M. Finally, we show *via* modeling that nanosheet assembly occurs by growth from a negligibly small critical nucleus. We also chart the dynamics of nanosheet size over a variety of conditions. Our results demonstrate control of the dynamics and size of the self-assembly of a nanostructured lattice, the constituents of which are one of a class of building blocks able to form novel hybrid nanomaterials.
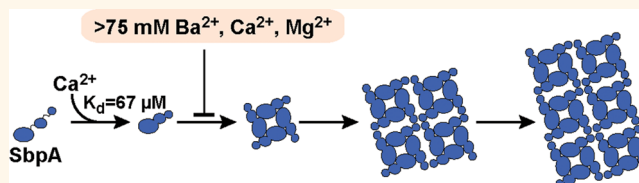
KEYWORDS: protein interactions · biomaterials · nanostructures · self-assembly dynamics · Ca^{2+} binding

Self-assembly is one of the most promising strategies for the creation of defined nanostructures. Naturally occurring protein assemblies are excellent starting points for developing these strategies because these assemblies present a range of shapes and symmetries.[1] However, controlling protein self-assembly to precisely create nanostructures requires an understanding of thermodynamic and kinetic factors governing their assembly, posing two significant challenges. First, the structure of protein assemblies arises from heterogeneous weak interactions that are very sensitive to pH and ionic strength.[2,3] Second, even small changes in protein interactions can lead to large changes in the dynamics of protein association.[4−6] Thus, to date most self-assembling systems do not allow tunable size control and do not display long-range order over microns. To create designer nanostructures we must first understand the effects of varying protein interactions on the mechanism and dynamics of protein self-assembly. Here we clarify these controls for the self-assembly of surface-layer (S-layer) proteins into nanosheets.

S-layers are one of the most abundant biological proteins. They self-assemble to form two-dimensional (2D) crystalline nanosheets with a variety of lattice symmetries and pore sizes in different organisms.[7] S-layer proteins do not self-assemble within the cell, but do so rapidly when exported to the cell surface.[8,9] Thus, S-layers can be expressed and purified at much higher levels (up to 10% of the protein of a cell[2,7,9]) than can most other self-assembling proteins, whose tendency to aggregate within the cell complicates protein expression and purification. S-layer lattice spacings are similar to the dimensions of quantum dots and nanotubes, and chemical groups or fusion proteins can be appended to S-layers without destroying

their ability to crystallize.[10−14] S-layer proteins therefore represent a useful set of building blocks for the creation of nanostructured arrays of organic and inorganic materials in a "bottom-up" fashion.[13,15] Lastly, given that they self-assemble readily as part of their biological function, S-layers are a compelling model system for understanding the interactions involved in protein self-assembly into nanostructures.[16,17]

SbpA, the S-layer protein from the insect pathogen *Lysinibacillus sphaericus*, has been engineered frequently for nanomaterials research. SbpA forms a one-protein-thick crystalline membrane (nanosheet) with square symmetry and a 15 nm protein tetramer unit cell. Assembly can take place on various solid supports and in solution in a Ca^{2+}-dependent fashion.[12,18,19] Self-assembly by SbpA is also affected by changing the ionic strength of the solution. Pum and Sleytr[16] showed that varying the concentration of Ca^{2+} ions affects the morphology of SbpA nanosheets. More recently Teixeria and colleagues found that the observed rate constant of SbpA assembly decreases with increasing Na^+ concentration, and shows a nonmonotonic dependence on the concentration of Ca^{2+}.[20] These experiments suggest that the self-assembly dynamics and morphology of SbpA is affected by the screening of interacting charged groups on the protein monomers by the divalent cation.

Despite these considerable advances, precise control of SbpA nanosheet formation has not been realized. We therefore sought to determine precise controls of the dynamics of nanosheet self-assembly by investigating the effect of divalent ion and protein concentrations using light scattering. By comparing high-throughput light scattering results with high-resolution electron microscopy (EM), we established that light scattering can efficiently map nanosheet yield and size as a function of time and ion concentration. In addition, we examined the effects of substituting Ca^{2+} for other cations to distinguish between a chemically specific and generic divalent cation role for Ca^{2+}. We found that Ca^{2+} mediates both specific and nonspecific interactions during self-assembly, resulting in a localized region in which nanosheet yield is optimal. Using the luminescence of Tb^{3+} binding to SbpA, we determine that 5 Tb^{3+} ions bind per monomer of SbpA. Then, we used competition experiments with Ca^{2+} to measure a binding affinity for the divalent cation. Finally, we correlate the time evolution of our light-scattering signals with a mechanism of irreversible growth from a negligibly small nucleus. Together, our results clarify external controls that trigger and inhibit SbpA self-assembly and chart the time-dependent yield and size of protein nanosheets.

RESULTS AND DISCUSSION

Light Scattering Experiments Measure Growth of Nanosheets of SbpA. While the self-assembly of SbpA can be measured

ex situ by scanning transmission electron microscopy (STEM) or atomic force microscopy (AFM), the throughput of these techniques is too low to allow monitoring of self-assembly yield and dynamics over a wide range of conditions. Therefore, we turned to static light scattering, which can monitor multiple reactions simultaneously and has been used extensively to monitor protein-based self-assembly processes.[21,22] In the absence of Ca^{2+}, purified monomers of SbpA did not self-assemble into nanosheets, and these solutions did not display an increase in light scattering at 340 nm over 800 min (Figure 1A, dotted line). In contrast, triggering self-assembly of 6.8 μM SbpA with addition of 10 mM Ca^{2+} (solid line) resulted in monomers forming into nanosheets as shown by STEM and small-angle X-ray scattering (SAXS) measurements (Figure S1, Supporting Information) and showed a sigmoidal increase in light scattering over time (Figure 1A). To correlate this light-scattering trend to the size and structure of self-assembling objects, we imaged samples from these solutions (time points indicated by colored circles in Figure 1A) using STEM with negative staining. For all time points, we primarily observed square sheets (*e.g.*, Figure 1B). The distribution of the side length of these sheets (Figure 1C) indicates that the average side length increased ~6-fold from 0.4 ± 0.1 μm at 50 min to 2.3 ± 0.7 μm at 800 min (Figure 1D). Taken together, these data indicate that the growth of nanosheets is one source of the increase in light scattering.

However, the light-scattering intensity depends both linearly on the number of sheets in solution and nonlinearly on their size. To determine if the sigmoidal increase in light scattering could be explained predominantly by the growth of nanosheets, we calculated the light scattering from a protein nanosheet (see Methods) to convert the sheet size distributions measured with STEM to light-scattering signals, using a uniform index of refraction of 1.45 for the protein (see Methods). The calculated light-scattering signal showed the same time dependence as the experimentally determined light-scattering signal (Figure 2). This correlation strongly suggests that the growth of the crystalline sheets is sufficient to explain the sigmoidal shape. More broadly, these results establish that time-dependent light scattering provides a dynamic readout of the size of nanosheets under these conditions.

Mapping Relative Assembly Yield Reveals a "Sweet Spot" For Nanosheet Formation. Using the light-scattering assay, we sought to map out how simultaneous variations in SbpA and Ca^{2+} concentration affect the self-assembly dynamics of SbpA nanosheets. Across varying concentrations of SbpA and Ca^{2+}, we monitored the time-dependent evolution of the normalized A_{340nm} (A_{norm}, see Methods, for A_{340nm} see Table S1). A_{norm} as a function of protein and Ca^{2+} concentration for all time points and a subset of time points are shown in Movie S1 and Figure 3A, respectively. At early times, we
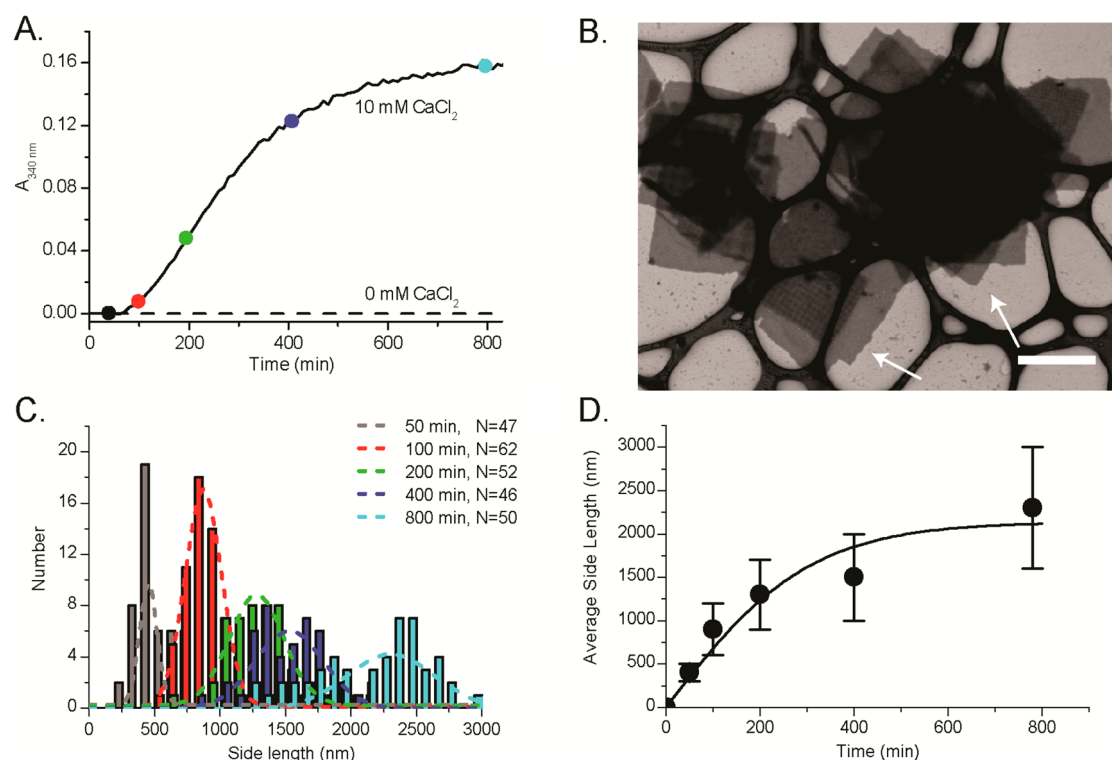
Figure 1. Light scattering is a measure of SbpA nanosheet growth in solution. (A) Representative traces of A_{340nm} *vs* time from light-scattering assays containing SbpA (6.8 μM) in solution in the absence (dashed line) or presence of 10 mM Ca^{2+} (solid line), indicating that increases in light scattering are associated with nanosheet formation. The colored, solid circles represent time points at which samples were imaged by STEM. (B) STEM images of negatively stained nanosheets of SbpA (6.8 μM) formed in the presence of 10 mM Ca^{2+} after 800 min. The white arrows point to stacks of square protein sheets. The scale bar represents 1 μm. (C) Histogram of the side lengths of sheets visualized by STEM at increasing reaction times. For each measurement, the total number of nanosheets measured (N) is indicated. The dashed curves represent Gaussian fits to each data set. (D) The side lengths of nanosheets as a function of time, indicating the growth of sheets with time. The average and standard deviation of the side length are determined from the Gaussian fits shown in C. The solid line is a fit of eq 6 to the data.
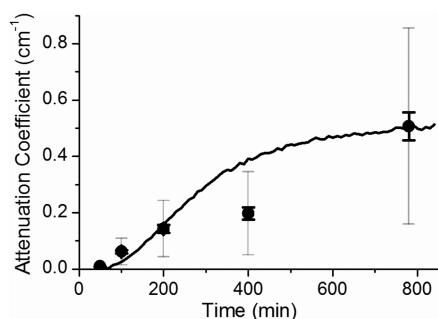

Figure 2. Scattering by growing nanosheets is sufficient to describe the sigmoidal behavior in light scattering. Plot of the attenuation coefficient measuring self-assembly of SbpA into nanosheets at a concentration of 6.8 μM with a Ca^{2+} concentration of 10 mM is shown. The calculated scattering values from the mean size and error of nanosheets of SbpA from Figure 1D are overlaid as closed circles with the standard error of the mean shown in black and the standard deviation shown in gray.

observed the highest A_{norm} at high protein concentrations and intermediate Ca^{2+} concentrations (100 min, Figure 3A, left panel). At intermediate and late times, the highest values for A_{norm} shifts to the center of the diagram, at intermediate values of both protein and Ca^{2+} concentration (400 min, Figure 3A, middle panel).

At the end point of the reaction (780 min, Figure 3A, right panel), the largest values for A_{norm} occurs at the optimal conditions of 7 μM SbpA and 10 mM Ca^{2+}. We observed no significant light scattering for concentrations of SbpA less than 3 μM. A_{norm} dropped off with either an increase or decrease in the concentration of Ca^{2+} from this optimal concentration and there is no significant light scattering for concentrations of SbpA less than 3 μM.

To confirm that nanosheet abundance correlated with A_{norm}, we first used STEM to examine the protein structures formed at three Ca^{2+} concentrations with distinctly different values of A_{norm} at the reaction end point (Figure 3A, right panel, white circle, square, and triangle). Large nanosheets were abundant from the solution with a high A_{norm} (Figure 3B, middle panel), but few sheets were observed from solutions with 4- and 18-fold lower values of A_{norm} (Figure 3B, left and right panels, respectively). Next, we measured solution scattering using SAXS of reaction end point samples with three Ca^{2+} concentrations and different A_{norm} (Figure S2). By probing all the species in solution, not just species that are retained on a STEM grid chip, SAXS provides a broader view of the self-assembly products than STEM. In the solution with the highest
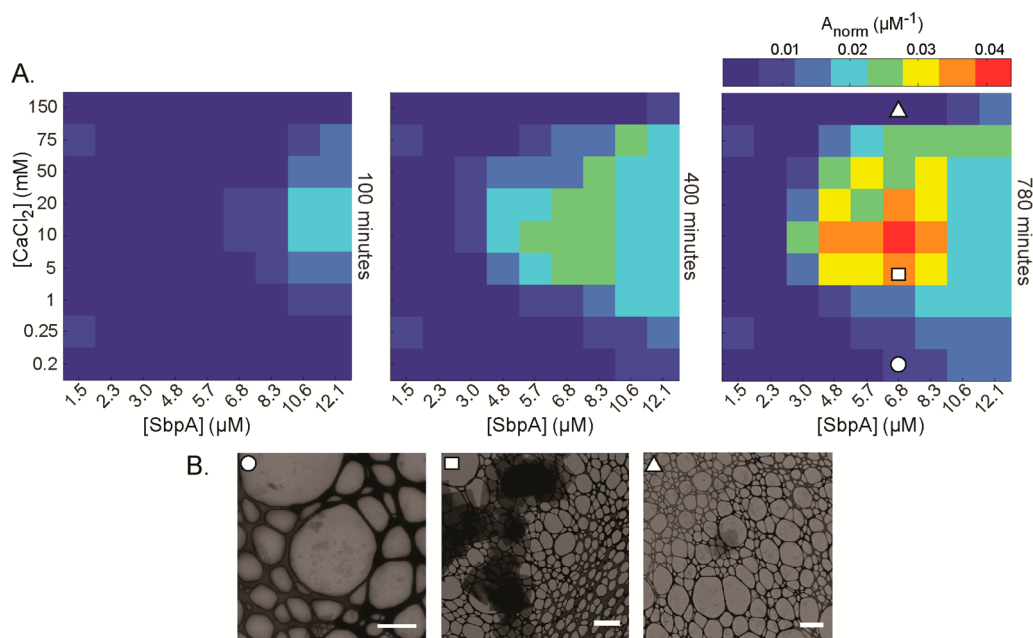
Figure 3. The dynamics and yield of nanosheets of SbpA are dependent on both the protein and Ca^{2+} concentration. (A) Normalized A_{340nm} (A_{norm}) as a function of Ca^{2+} and SbpA concentration at 100 (left panel), 400 (middle panel), and 780 min (right panel) after starting the reaction. At 780 min, the data show a localized region of nanosheet assembly. The color scale indicates the value of A_{norm} (calculated as detailed in Methods) and is identical for each panel. (B) Representative STEM images of SbpA reactions at three different Ca^{2+} concentrations: 0.25 mM (circle), 5 mM (square), and 150 mM (triangle). The scale bar represents 2 μm for the left and middle panel and 4 μm for the right panel.

A_{norm}, we observed a Bragg peak at a q-value of 0.05 Å^{-1}, corresponding to a repeat spacing of the crystalline lattice of SbpA nanosheets. This peak appears broader in solutions with 60-fold and 20-fold lower A_{norm}, indicating that nanosheets are smaller or less structured. Thus, these observations by SAXS and EM strongly support that A_{norm} is a metric for the size and number of nanosheets, which we refer to as the relative assembly yield of nanosheets.

Using A_{norm} as a measure of relative assembly yield in this succession of diagrams (Figure 3A) gives rise to three distinct observations. First, at SbpA concentrations above 3 μM there is a limited range of Ca^{2+} concentrations that give many large S-layer nanosheets at the reaction end point (Figure 3A, right panel). At Ca^{2+} concentration between 1 and 50 mM, nanosheets are abundant, as indicated by the high end point A_{norm}. At Ca^{2+} concentrations ≤ 1 mM and ≥ 75 mM, the A_{norm} after 780 min was low, indicating few or very small nanosheets are present. Second, at SbpA concentrations less than 3 μM the low A_{norm} values indicate that small and/or few nanosheet self-assemble in solution. Third, for all self-assembly reactions that had a high assembly yield, A_{norm} increased in a sigmoid fashion with time. Below, we further investigate these observations to understand controls on and mechanisms underlying the nanosheet self-assembly process.

Nanosheets Do Not Form below a Threshold SpbA Concentration. We observed low light scattering at SbpA concentrations less than 3 μM (Figure 3A). To determine
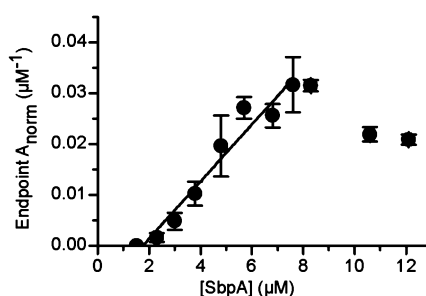

Figure 4. Formation of SbpA nanosheets in solution requires a minimum amount of free protein monomer. The end point A_{norm} plotted as a function of the SbpA concentration at 50 mM Ca^{2+} (black circles). The error bars represent the standard deviation of at least 3 measurements. The critical concentration of SbpA was determined by fitting a line through the data, and determining the intercept with the x-axis.

the threshold concentration for nanosheet assembly at 50 mM Ca^{2+}, we analyzed the end point A_{norm} as a function of SpbA concentration (Figure 4). The end point A_{norm} is zero for SbpA concentrations ≤ 1.5 μM and increases roughly linearly from 2.3 to 7.8 μM. From a linear fit of the latter data points we estimate a threshold concentration of 1.8 ± 0.2 μM. This value represents the lowest concentrations where we can observe nanosheet self-assembly over 780 min and is thus an upper bound for concentration below which all nanosheets would dissolve.

Ca^{2+} Has a Dual Role on the Relative Assembly Yield Due to Ion-Specific and Divalent Cation Roles. Since Ca^{2+} can induce

a conformational change within S-layer proteins[18,23,24] and has been suggested to mediate electrostatic interactions between S-layer monomers,[20] we hypothesized that Ca^{2+} might be affecting self-assembly both in an ion-specific manner and more generally as a divalent cation. To test whether other divalent cations could stimulate self-assembly, we first monitored the A_{340nm} in self-assembly reactions in which we added 5 mM Mg^{2+} or Ba^{2+} instead of Ca^{2+} to purified SbpA solutions. We observed no increase in light scattering with Ba^{2+} or Mg^{2+}, indicating that neither divalent ion stimulated self-assembly (Figure S3). Next, we replaced Ca^{2+} with Tb^{3+}, which can bind in place of Ca^{2+} in many Ca^{2+} binding proteins due to its similar ionic radius.[25] In this case, we find that the scattering signal increased similarly to the condition in which Ca^{2+} was used (Figure S3A,B). However, observing the structures from the Tb^{3+} reactions by STEM revealed the presence of only small aggregates, not nanosheets (Figure S3C). These observations indicate that Ca^{2+} has an ion-specific role in triggering self-assembly of nanosheets.

Next, we titrated the different cations (Ca^{2+}, Mg^{2+}, Ba^{2+}) in the presence of 5 mM Ca^{2+} and 7.8 μM SbpA and measured the A_{340nm} after 780 min as a function of total cation concentration (Figure 5A). In the Ca^{2+}-only reactions, we observed an increase in the A_{340nm} up to 10 mM Ca^{2+}, at which point increasing the Ca^{2+} concentration results in a decrease in this value (Figure 5A, blue circles). We found quantitatively similar behavior (within error bars) for the mixed Mg^{2+} and Ca^{2+} titrations (Figure 5A, black circles), and qualitatively similar behavior for the mixed Ba^{2+} and Ca^{2+} titrations (Figure 5A, red circles). In the titrations with Ba^{2+}, light scattering decreased after 5 mM and remained somewhat lower than in the other two cases. These observations indicate that above a concentration of 5 mM, the effects of Ca^{2+} on SbpA nanosheet self-assembly can be mimicked by other divalent cations.

As another test that the decrease in nanosheet formation is dependent on the overall divalent cations in solution and not due to a specific cation, we performed a series of self-assembly experiments in which the total ion concentration of the solution was held constant at 50 mM, but the relative amounts of Mg^{2+} and Ca^{2+} were varied (Figure 5B). In these experiments, we observed no significant change in the end point absorbance values as a function of the Mg^{2+}-to-Ca^{2+} ratio, fitting a line to the yield-versus-time data with a negligible slope. Taken together, our data indicate that Ca^{2+} promotes SbpA nanosheet assembly *via* an ion-specific effect at concentrations less than 5 mM Ca^{2+}. However, above this concentration, the effects of Ca^{2+} on self-assembly can be replicated by other divalent cations; these cations first promote SbpA self-assembly then inhibit it at concentrations of 10 mM or above.
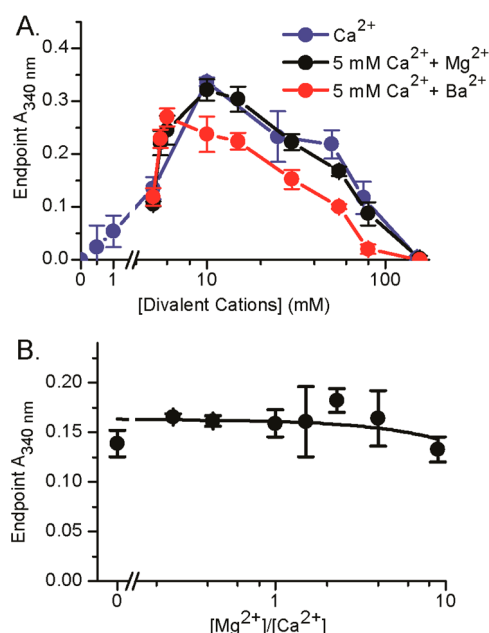

Figure 5. Formation of SbpA nanosheets in solution is not linearly dependent on the divalent ion concentration. (A) End point absorbance measurement from light scattering assays as a function of the divalent cation concentration for Ca^{2+} only (blue circles), 5 mM Ca^{2+} + Mg^{2+} (black circles), or 5 mM Ca^{2+} + Ba^{2+} (red circles). (B) End point absorbance measurements from light scattering experiments in which the total divalent ion concentration was kept at 50 mM total, while varying the relative concentrations of Ca^{2+} and Mg^{2+}. A linear fit of the data gives a slope of -10^{-3} (black line). The x-axis is linearly scaled before the break, and is on a logarithmic scale after the axis break. Error bars represent standard deviation from 2 to 3 measurements.

Although our light scattering data show that minimally 1 mM Ca^{2+} is needed to specifically stimulate self-assembly of SbpA, this value does not represent a binding constant of SbpA for Ca^{2+}. To measure the affinity of SbpA to Ca^{2+} we used Tb^{3+} luminescence as an indicator to measure the formation of protein-ion complexes.[25,26] First we determined whether SbpA can bind Tb^{3+}, resulting in a luminescent signal when the tryptophan residues in the protein are excited. When we excited SbpA-Tb^{3+} complexes with 280 nm light, we observed several emission peaks consistent with the peaks for Tb^{3+} luminescence (Figure 6A).[26] This spectrum indicates that Tb^{3+} binds SbpA and that at least one tryptophan residue is nearby (SbpA has six total), which when excited with 280 nm light results in luminescence from the Tb^{3+}.

We then used this luminescence signal to measure the binding affinity of Tb^{3+} to specific sites on SbpA. We titrated Tb^{3+} in the presence of 1.5 μM SbpA, a concentration at which nanosheet self-assembly does not occur, and followed the emission intensity at 544 nm when the protein-ion complex was excited at 280 nm (Methods). We observed a linear increase in the luminescence signal up to 5 μM Tb^{3+} at which point the signal reached a plateau (Figure 6B). We fit a single site binding curve eq 2 to the data to determine an
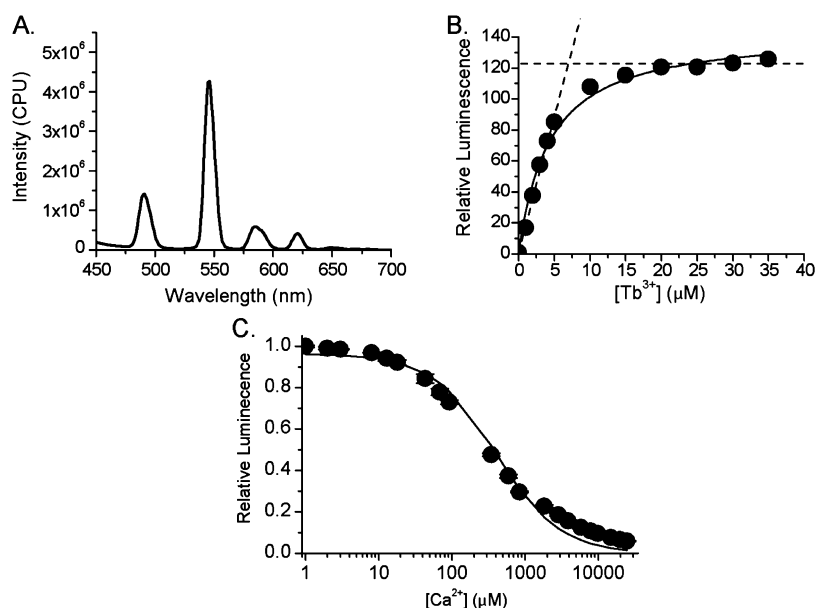
Figure 6. Tb^{3+} luminescence can measure binding of SbpA to Ca^{2+}. (A) A solution of SbpA (6.8 μM) with 10 mM Tb^{3+} was excited at 280 nm and the emission of the sample was observed from 450 to 700 nm. Four peaks are observed at 490, 546, 585, and 620 nm, indicating that Tb^{3+} binds to SbpA. (B) Titration binding curve of Tb^{3+} to 1.51 μM SbpA as measured by Tb^{3+} luminescence. The complex was excited at 280 nm and the emission observed at 544 nm. The solid circles represent data points and the solid line is a fit of a one-site binding curve to the data. The dashed lines are fits to linear portions of the data. The intersection of the dashed lines was used to determine the stoichiometric break-point for this binding curve. (C) Competition of Tb^{3+}-SbpA complexes with Ca^{2+} as measured by a decrease in the Tb^{3+} luminescence. The open circles are titration data, which are fit by a competition binding curve shown by a solid line. The error bars represent the standard deviation determined from two experiments.

apparent affinity of SbpA for Tb^{3+}[27] and calculated a $K_{d,\text{Tb}^{3+}} = 7 \pm 1$ μM (Methods). Moreover, from the intersection of linear interpolations of the data at the plateau and the initial linear increase, we calculated a stoichiometery of 4.7 ± 0.5 Tb^{3+} per SbpA monomer.

To determine a binding constant specific for Ca^{2+}, we next performed a competition experiment in which the solution of Tb^{3+} and SbpA from the previous experiment was titrated with increasing concentrations of Ca^{2+} to compete for the binding sites. Figure 6C shows a competition experiment in which we observed the luminescence signal from Tb^{3+} bound to SbpA decrease as the total concentration of Ca^{2+} increases. We fit the data to eq 3 (see Methods)[28] and determined an apparent dissociation constant $K_{d,\text{Ca}^{2+}}$ of 67.1 ± 0.3 μM of SbpA for Ca^{2+}.

Structural studies of another S-layer protein, *Geobacillus stearothermophilus* SbsB, provide a model to explain the dual roles of Ca^{2+} in stimulating self-assembly by SbpA. In the absence of Ca^{2+}, both SbsB and SbpA exist in an extended form.[23,29] In the presence of Ca^{2+}, monomers of SbsB bind four structural Ca^{2+} ions that increase the tertiary structure in SbsB.[23] We propose that, similar to SbsB, SbpA may specifically coordinate several Ca^{2+} ions upon their addition, causing the monomer to adopt a tertiary structure that triggers self-assembly. We observe that Ca^{2+} binds SbpA with an affinity (67 μM) that is within the same magnitude of that reported for SbsB ($\sim$100 μM). Moreover, we find that 5 Tb^{3+} bind per monomer of SbpA,

suggesting that there are at least 5 binding sites for Ca^{2+}. The crystal structure of SbsB shows that four Ca^{2+} are bound by the monomers, which mediate interdomain contacts.

In a second effect, ion-mediated interactions *between* monomers may alter the rate and yield of self-assembly. To test whether ions affect the charge of SbpA we carried out zeta potential measurements of SbpA in various solutions. The theoretical pI of the protein is calculated to be 4.81.[30] Indeed in water the protein monomer is negatively charged (Figure S4). In pH 7.2 buffer and 100 mM NaCl the protein charge increases, but is still negative. However, with the addition of Ca^{2+} or Mg^{2+}, we observe a neutral charge on the protein (Figure S4). Charged residues such as aspartic acid, glutamic acid, and lysine are proposed to be involved in the interaction between the monomers of SbsB nanosheets,[23] suggesting that similar interaction occur between SbpA monomers. The nonmonotonic dependence of light scattering on divalent cation concentration in Figure 5A and our zeta potential measurements suggest that moderate concentrations of divalent cations, including Ca^{2+}, may induce counterion-mediated attraction between negatively charged sites,[20,31] while high concentrations may induce overcharging of those sites.

The role of Ca^{2+} elucidated here may explain how the cell controls SbpA self-assembly *in vivo*. While S-layer proteins do not self-assemble intracellularly, they must crystallize on the extracellular surface at an

estimated rate of 500 monomers/s to maintain a 2D array during cell division.[32] The internal Ca^{2+} concentration for bacterial cells appears to be highly regulated, although it has not been widely measured. Assuming *L. sphaericus* has same the internal Ca^{2+} concentration as *Escherichia coli*, *i.e.*, 0.1– 0.3 μM,[33,34] the intracellular concentration of Ca^{2+} would be far too low to induce rapid self-assembly by SbpA given a dissociation equilibrium constant of 67 μM. However, when the protein is excreted into the extracellular space where the concentration of Ca^{2+} is typically in the millimolar range,[35] SbpA would rapidly self-assemble on the bacterial surface.

The Dynamics of Self-Assembly of SbpA Map out the Time-Evolution of Nanosheet Size and Are Consistent with Irreversible Growth from a Negligibly Small Nucleus. Because light scattering gives a dynamic readout of the nanosheet growth, we sought to predict nanosheet size over the range of solution conditions examined above and develop a mechanism for self-assembly. Since we established that the observed increase in light scattering signal is predominantly due to growth of nanosheets (Figure 1), we inverted our dielectric calculation (using a uniform protein index of refraction as the only adjustable parameter) to calculate nanosheet size as a function of the ionic strength of the solution and time. Figure 7A illustrates the range of lengths of nanosheets at each [SbpA] and [Ca^{2+}] after 780 min as determined from the light scattering values. These diagrams provide a guide for creating SbpA nanosheets of a distribution of sizes by varying the ionic strength of the solution and the reaction time.

Because of the lack of a long lag time prior to sheet growth, we hypothesized that the light scattering trace from solutions of SbpA and Ca^{2+} might be explained by the irreversible growth of square nanosheets (Figure S5). We developed a model for the irreversible growth of planar sheets (see Methods), which assumes that some fraction f of proteins serve as sites where nanosheet formation initiates; subsequent nanosheet growth is driven by diffusion of proteins onto the perimeter of the sheets, where their attachment is characterized by an effective cross section per monomer, σ. As discussed in the Methods section, we combined this model with our dielectric calculation to give the time dependence of A_{norm}, using f and σ as adjustable parameters in least-squares fits for each solution condition. Since the model assumes that all monomers become incorporated into sheets at long times, the long-time sheet length $L(\infty)$ is proportional to $f^{1/2}$.

We found that our model could successfully fit time traces for a broad range of solution conditions, as illustrated by the dashed lines in Figure 7B for 50 mM Ca^{2+} and SbpA concentrations ranging from 4.8 to 12.1 μM SbpA. We did not fit traces from concentrations below 4.8 μM because the time courses were not
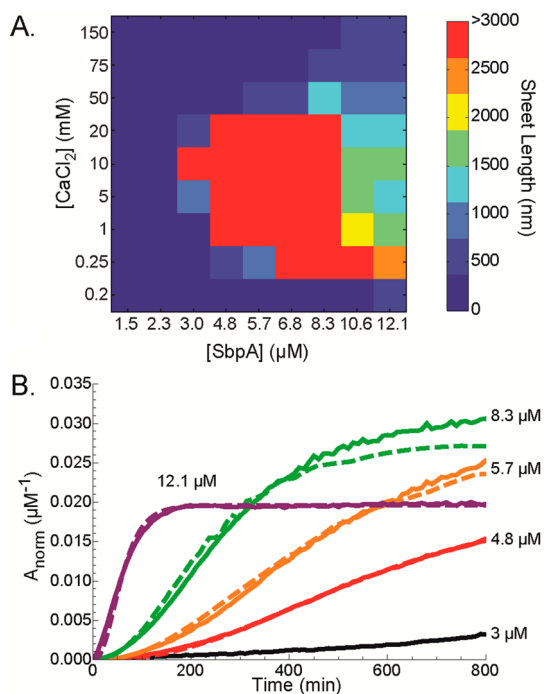

Figure 7. Self-assembly by SbpA corresponds to irreversible growth. (A) Estimated sheet lengths from the end point light scattering data are plotted as a function of the [Ca^{2+}] and [SbpA] at 780 min (Figure 2A). The lengths were calculated using the equation for scattering by dielectric discs and using a sheet thickness of 10 nm. The color map is capped at 3000 nm due to the variability of the lengths calculated with high light scattering. **(B)** A_{norm} as a function of time for SbpA self-assembly at 50 mM Ca^{2+} and increasing protein concentration (colored curves). Fits to eq 4 are shown as dashed curves in the same color.

long enough to exhibit a sigmoid shape necessary to constrain the fit. Using the best-fit values of f (Table S2) to calculate $L(\infty)$, the length of sheets at long times, we find that the values for $L(\infty)$ have a range and variation of 4 $\pm$ 2 μm over conditions where we observed sigmoidal light scattering behavior. These sheet lengths are consistent with the end point sheet sizes observed in the STEM images. In addition, we find that the best-fit values for σ are similar in value for all protein concentrations, with an average value of 2.5 $\pm$ 0.7 $Å^2$. This cross section of 2–3 $Å^2$ is consistent with an interaction range between functional groups on the protein, such as charged residues, which are important in the kinetics of protein–protein association.[36] Finally, we note that our model assumes irreversible growth from a negligibly small nucleus. The quality of the fits demonstrates that a substantial nucleation barrier is not necessary to explain the sigmoid shape of the light scattering traces; rather, the sigmoid shape is a natural consequence of the nonlinear dependence of light scattering on sheet size.

CONCLUSION

Establishing and using light scattering as a proxy for nanosheet formation by SbpA, we determined how

varying the concentrations of Ca^{2+} and SbpA affect the yield of nanosheets and the temporal evolution of nanosheet size. We found that the relative yield of self-assembly is affected nonmonotonically by the Ca^{2+} concentration. Tuning the identity and concentration of divalent cations indicated that Ca^{2+} plays two roles in mediating assembly: a Ca^{2+}-specific role likely associated with conformational changes within a protein and a generic role as a divalent cation likely associated with mediating interactions between proteins. Additionally, by inverting a dielectric calculation to determine sheet size as a function of time, $[Ca^{2+}]$, and $[SbpA]$, we find that the time evolution of the light scattering traces is consistent with irreversible growth of sheets from a negligibly small nucleus. Our results highlight the usefulness of mapping out diagrams for understanding self-assembling systems and indicate several means to control the size and morphology of SbpA-based nanostructures.

Previously, solution controls on protein self-assembly have been mapped out using phase diagrams constructed using end point turbidity measurements.[37] The diagrams and model presented here go beyond this previous work by determining the time-dependent evolution of nanosheet size as well of mechanistic controls on assembly yield. Thus, we suggest that such diagrams coupled with modeling of the self-assembly process may provide a useful method to determine critical kinetic controls of proteins and polymers into nanostructures. Additionally, our results identify conditions to initiate and halt self-assembly to produce SbpA nanosheets of an average size in high yield. This information provides a first example of using self-assembly to tune the size of 2D protein nanostructures with long-range order and will be useful for patterning inorganic nanomaterials at defined length scales, potentially opening the door to efforts to design self-assembling multicomponent, mesoscale S-layer lattices.

METHODS

SbpA Expression and Purification. SbpA was purified as previously described.[38] After being denatured from purified cell wall fractions using a solution of 50 mM Tris HCl pH 7.2, and 5 M guanidine hydrochloride, SbpA was dialyzed extensively into Milli-Q water (EMD Millipore, Billerica, MA), which has a resistivity of 18 MΩ·cm and TOC of 5 ppb. Aggregated protein was removed by a final centrifugation at 100000g at 4 °C in an Optima L-100XP ultracentrifuge (Beckman Coulter, Brea, CA) using the SW41 Ti rotor. Protein concentrations were determined through Beer's law using the calculated molar extinction coefficient at 280 nm of 78 940 M^{-1} cm^{-1} or the weight extinction coefficient of 0.6 $(mg/mL)^{-1}$ cm^{-1}.[39] In agreement with previous reports,[19,29,40] purified SbpA was present as a monomer with a hydrodynamic diameter of 11.7 ± 0.5 nm (Figure S1A,B), and upon addition of 10 mM Ca^{2+}, the protein crystallized into a porous, square lattice with a cell spacing of 13.2 ± 0.2 nm (Figure S1C).

Light Scattering Assay. Because of the absorption of light by proteins at lower wavelengths, nanosheet self-assembly by SbpA was monitored *via* the scattering of light at 340 nm.[22] Absorbance was monitored using a Spectra Max 384 plus plate reader equipped with temperature control (Molecular Devices, Sunnyvale, CA). Reactions (100 μL) were performed in self-assembly buffer (10 mM Tris HCl pH 7.2, 100 mM NaCl) and the indicated concentration of SbpA, $CaCl_2$, $MgCl_2$, or $BaCl_2$. All buffers were made using Milli-Q water. Solutions were mixed and then added into wells on a Costar UV clear, 96-well flat bottom plate and covered with an optically clear seal to prevent evaporation (Corning Inc. Corning, NY). The reactions were incubated at 25 °C, and prior to measuring absorbance at each time point, the plate was mixed for 1 s by shaking. The calculated path length for each well is 2.9 mm, based on the cylindrical shape of the well with an average radius of 3.32 mm, and the volume of solution. Data were corrected by subtracting the absorbance at zero time, A_{340nm,t_0}. Data were exported to and analyzed in Origin 8.5.0 (OriginLab, Northampton, MA.). To plot diagrams, the data were imported into MATLAB v7.9.0.529 R2009b (The MathWorks, Natick, MA) and plotted using the "imagesc" plot function. The normalized absorbance at 340 nm (A_{norm}) was calculated by using the relation, $A_{norm} = (A_{340nm,t} - A_{340nm,t_0})/[SbpA]_{tot}$, where $A_{340nm,t}$ is the absorbance at time t and $[SbpA]_{tot}$ is the total protein concentration.

Electron Microscopy. To prepare *ex situ* samples for STEM, SbpA (6.8 μM) was incubated for the indicated time at 25 °C in self-assembly buffer, and the indicated concentration of

$CaCl_2$. Solutions of SbpA crystals were diluted by 5-fold into Milli-Q water, and 8 μL of this dilution was immediately pipetted onto 400 Cu mesh grids, with a thin carbon film (Ted Pella Inc., Redding, CA). The solution of SbpA was incubated for 2 min at room temperature on the grid. The drop was removed by absorbing the liquid with filter paper. The grid was washed twice by pipetting Milli-Q water on the surface, then removing excess liquid with filter paper. Finally, the protein sheets were stained for 2 min with one drop of NanoW solution (Nanoprobes Inc., Yaphank, NY) and allowed to dry for 16 h after absorbing the excess solution from the grid with filter paper. Samples were imaged on a FESEM ULTRA 55 electron microscope (Carl Zeiss Microscopy, Thornwood, NY) in STEM mode at a voltage of 30 kV. Images were captured using SmartSEM software. Length measurements and 2D Fourier transforms were performed using NIH ImageJ software (http://imagej.nih.gov/ij/index.html) v1.47a.[41] Because many sheets stack on top of one another at higher concentrations of SbpA, making it difficult to quantify the area of individual sheets, we measured the side lengths of individual sheets to assess the size of sheets. The histogram of SbpA crystal lengths were plotted and fit to a Gaussian distribution in Origin 8.5.0.

Dynamic Light Scattering (DLS) and Zeta Potential Measurements. Dynamic light scattering measurements were taken on a Zetasizer nano-ZS (Malvern Instruments, Worcestershire, United Kingdom). For DLS, reactions of SbpA in self-assembly buffer (100 μL) were pipetted into a disposable solvent resistant microcuvette (Malvern Instruments, Worcestershire, United Kingdom), sealed with a plastic lid and PARAFILM, and then placed into the instrument. The temperature was equilibrated to 25 °C for 1 min, prior to acquisition of data. Throughout the measurement, the temperature was held constant at 25 °C. The size of the protein was measured by illuminating the sample with a 633 nm laser, and monitoring the scattered light 173° from the incident beam. The refractive index, n, of the protein was set to 1.450,[42] and the refractive index of the dispersant, water, was set to 1.330.[43] The viscosity of water at 25 °C, 0.8872 cP, was used for the calculation of the hydrodynamic diameter. Measurements were repeated 3 times for each sample, and replicated 2−3 times on different days.

Zeta potential measurements were performed in a 750 μL, disposable Zetasizer nano cells (Malvern). The cells were rinsed with 5 mL of 70% ethanol, 5 mL nanopure water. For solutions of protein in buffer, the cells were washed with a solution of 10 mM Tris HCl pH 7.2, 100 mM NaCl, 6.8 μM SbpA and the indicated concentration of $MgCl_2$ or $CaCl_2$. The cell was then filled with the

solution containing protein and sealed. Measurements were taken within 1−2 min of preparation, prior to formation of crystals in solution.

Small Angle X-ray Scattering (SAXS). Solutions with the indicated concentration of SbpA in self-assembly buffer and the indicated concentration of $CaCl_2$ were incubated at 25 °C for at least 16 h. Solutions (24 μL) were loaded onto a 96 well PCR microplate (Axygen Inc., Union City, CA) and sealed with an AxyMat sealing mat (Axygen Inc.). X-ray scattering experiments were conducted at the SIBYLS ALS beamline 12.3.1.[44] Data were analyzed and traces from 0.5 s and six second exposures were merged in PRIMUSv3.1 (http://www.embl-hamburg.de/biosaxs/manual_primus.html).[45] The merged data were plotted in Origin 8.5.0.

Calculating Light Scattering from Nanosheets. To calculate the light scattering signal as a function of nanosheet length, the square sheets were approximated as thin circular disks of equivalent cross section, thickness, and uniform dielectric constant. This approximation allows for the application of a known solution for the a scattering efficiency factor, Q, as detailed in the Supporting Information Methods.[46] We then calculated the light scattering *via* eq 1

$$A_{norm} = \frac{I\alpha}{\rho_m} = I\sigma_m \frac{\sum_L N(L)Q(L)L^2}{\sum_L N(L)L^2} \qquad (1)$$

where I is the sample depth, α is the attenuation coefficient, ρ_m is the protein monomer number density, σ_m is the physical cross section of a protein monomer, L is the sheet length, $N(L)$ is the number of sheets of length L, and $Q(L)$ is the scattering efficiency factor. The index of refraction for S-layer proteins is set to 1.450 in the calculation of Q (eq S1).

Tb^{3+} and Ca^{2+} Binding Titrations. To measure Tb^{3+} luminescence, spectra and emission readings were taken on a Fluoromax-4 Spectrofluorometer (Horiba Jobin YVON, Edison, NJ). Luminescence spectra were taken by adding 100 μL of sample to a 300 μL 3 × 3 mm QS microcell (Hellma, Müllheim, Germany). A 370 nm cutoff filter was mounted in front of the emission port in the instrument to prevent interference from harmonic doubling. The sample was illuminated at 280 nm with 5 nm slit-width. Emission spectra were collected using 5 nm slit width.

For binding titration of SbpA with Tb^{3+} 2 mL of a solution containing 1.5 μM SbpA in 10 mM Tris HCl pH 7.2 and 100 mM NaCl was added to a 10 × 10 mm QS 3500 mL cuvette along with a magnetic stir bar (Hellma, Müllheim, Germany). We used this concentration of SbpA to avoid self-assembly in solution and measure only the binding of ions to the proteins. The solution was stirred and equilibrated to 25 °C with a 1 °C tolerance. The solution was excited at 280 nm with a slit-width of 5 nm, and the emission was monitored at 544 nm after being filtered through a 370 nm cutoff filter. Stock solutions of 2 and 10 mM $TbCl_3$ in water were used to titrate the ion in solution. The solution was allowed to equilibrate for 1 min after each titration, and then the shutters were open to take a reading for 30 s. Fluorescence values were averaged per reading, and then corrected for dilution effects by multiplying the intensity by the ratio of the total volume (V_i) and the initial volume (V_0) such that $F_i = F(V_i/V_0)$. The values were then plotted by normalizing each titration point (F_i) to the initial fluorescence (F_0) resulting in a relative fluorescence change ($F_{rel} = F_i/F_0$). Two sets of data were individually fit using NLLS in Origin 8.5.1 to the equation for single site binding of a ligand to protein[27] given by

$$F_{rel} = \frac{\left(1 + \frac{[L_f]F_{ml}}{K_{d,Tb^{3+}}}\right)}{\left(1 + \frac{[L_f]}{K_{d,Tb^{3+}}}\right)} \qquad (2)$$

In eq 2 F_{rel} is the relative fluorescence change, F_{ml} is the fluorescence of the SbpA-Tb^{3+} complex, L_f is the free Tb^{3+} concentration and $K_{d,Tb^{3+}}$ is the dissociation equilibrium constant for Tb^{3+}. L_f is given by the solution to the quadratic equation involving the terms for total protein, total ligand and $K_{d,Tb^{3+}}$.[27] Only two parameters were varied, F_{ml} and $K_{d,Tb^{3+}}$.

Competition experiments were performed after titration with Tb^{3+}. For each experiment the solution contained the same total concentration of Tb^{3+}. Ca^{2+} was titrated over several concentration decades from stocks of 2, 10, 50, 500, and 1000 mM. The fluorescence was recorded and corrected as described above. The data were fit to the general solution for competitive binding of two ligands to a macromolecule.[28] That is the data were fit to eq 3,

$$F_{rel} = f_{max}[SbpA\text{-}Tb^{3+}] \qquad (3)$$

where f_{max} is the maximum relative luminescence of the SbpA-Tb^{3+} complex, and the [SbpA-Tb^{3+}] was determined by solving for the real roots of the cubic equation using Mathematica 7 (Wolfram Research, Champaign, IL) as a function of the total protein concentration, total concentration of Tb^{3+}, the total concentration of Ca^{2+}, the dissociation binding constant of SbpA for Ca^{2+}, $K_{d,Ca^{2+}}$, and $K_{d,Tb^{3+}}$.[28] The parameters $K_{d,Ca^{2+}}$ and f_{max} were varied to obtain a minimum value for the least-squares difference to the titration data.

Model Fitting to the Light Scattering Data. Light scattering data were imported into and fit to the equations described below in Mathematica 7 (Wolfram Research, Champaign, IL). The growth of sheets was modeled by assuming that a fraction f of proteins serves as nucleation sites, with subsequent growth driven by adsorption of proteins onto the perimeter of the sheets. The parameter f can be written as $a^2/(4L(\infty)^2)$, where $L(\infty)$ is the length of sheets at long times and a is the unit cell spacing. We assume that the growth of a sheet composed of $N(t)$ monomers is given by

$$\frac{d}{dt}N(t) = N_p(t)F\sigma(1 - fN(t)) \qquad (4)$$

where $N_p(t)$ is the number of monomers on the perimeter of the sheet, F is the diffusive flux of monomers onto the perimeter, and σ is the effective cross section per monomer. The last factor in eq 4 accounts for saturation when all monomers are incorporated into the growing sheet. The number of monomers of SbpA in a sheet can be written as $N(t) = 4(L(t)/a)^2$, and the number of monomers on the perimeter can be written $N_p(t) = 8L(t)/a$, assuming that two monomers are exposed at the edges. In this case eq 4 can be written as

$$\frac{d}{dt}L(t) = aF\sigma\left(1 - 4f\left(\frac{L(t)}{a}\right)^2\right) \qquad (5)$$

Since the diffusive flux of monomers onto the crystal edge is driven by the concentration gradient, we set $F = Dc/d$, where D is the diffusion coefficient, c is the protein concentration, and d is the depth of the depletion layer characterizing the concentration gradient.[47] Because the diffusive flux is faster than sheet growth (see below), only the adsorbing perimeter, not the bulk of the sheet, is expected to maintain a steady-state concentration gradient. Balancing the number of monomers on the perimeter with the number removed from within the depletion depth layer[47] yields an estimate of $d = (8/(\pi ac))^{1/2}$ for the depletion depth. Combining the above results and integrating eq 5 yields the following solution for sheet size:

$$L(t) = \frac{a}{2\sqrt{f}}\tanh\left(\left(\frac{\pi c^3 af}{2}\right)^{1/2}\sigma Dt\right) \qquad (6)$$

eq 6 was first fit to the sheet size data in Figure 1D, resulting in an effective cross section of $\sigma = 1.4 \pm 0.3$ Å^2 and a nucleation site density of $f = 1.2(\pm 0.6) \times 10^{-5}$. These parameters were then used in fits of the light scattering calculation eq 1 to the light scattering data to determine the best-fit protein index of refraction. We checked the consistency of our assumption that the diffusive flux is rapid by verifying that the time scale for diffusion across the depletion depth, $\tau_d = d^2/(2D)$, is much smaller than the time scale for a sheet growing across the depletion depth, defined by $L(t + \tau_g) - L(t) = 2d$. At $c = 6.8$ μM, we found τ_d to be on the order of 10^{-4} s, and τ_g to indeed be much larger, on the order of 1 h. We did not fit traces from concentrations below 4.8 μM SbpA because the time courses

were not long enough to exhibit a sigmoid shape necessary to constrain the fit.

REFERENCES AND NOTES

1. Pavkov-Keller, T.; Howorka, S.; Keller, W. The Structure of Bacterial S-Layer Proteins. *Prog. Mol. Biol. Transl. Sci.* **2011**, *103*, 73–130.
2. Pum, D.; Toca-Herrera, J. L.; Sleytr, U. B. S-Layer Protein Self-Assembly. *Int. J. Mol. Sci.* **2013**, *14*, 2484–2501.
3. Brodin, J. D.; Ambroggio, X. I.; Tang, C.; Parent, K. N.; Baker, T. S.; Tezcan, F. A. Metal-Directed, Chemically Tunable Assembly of One-, Two- and Three-Dimensional Crystalline Protein Arrays. *Nat. Chem.* **2012**, *4*, 375–382.
4. Vekilov, P. G. The Two-Step Mechanism of Nucleation of Crystals in Solution. *Nanoscale* **2010**, *2*, 2346–2357.
5. Whitelam, S. Control of Pathways and Yields of Protein Crystallization through the Interplay of Nonspecific and Specific Attractions. *Phys. Rev. Lett.* **2010**, *105*, 088102.
6. Haxton, T. K.; Whitelam, S. Design Rules for the Self-Assembly of a Protein Crystal. *Soft Matter* **2012**, *8*, 3558–3562.
7. Sleytr, U. B.; Schuster, B.; Egelseer, E. M.; Pum, D.; Horejs, C. M.; Tscheliessnig, R.; Ilk, N. Nanobiotechnology with S-Layer Proteins as Building Blocks. *Prog. Mol. Biol. Transl. Sci.* **2011**, *103*, 277–352.
8. Fagan, R. P.; Fairweather, N. F. Biogenesis and Functions of Bacterial S-Layers. *Nat. Rev. Microbiol.* **2014**, *12*, 211–222.
9. Engelhardt, H.; Peters, J. Structural Research on Surface Layers: A Focus on Stability, Surface Layer Homology Domains, and Surface Layer-Cell Wall Interactions. *J. Struct. Biol.* **1998**, *124*, 276–302.
10. Badelt-Lichtblau, H.; Kainz, B.; Vollenkle, C.; Egelseer, E. M.; Sleytr, U. B.; Pum, D.; Ilk, N. Genetic Engineering of the S-Layer Protein SbpA of *Lysinibacillus sphaericus* CCM 2177 for the Generation of Functionalized Nanoarrays. *Bioconjugate Chem.* **2009**, *20*, 895–903.
11. Ilk, N.; Kupcu, S.; Moncayo, G.; Klimt, S.; Ecker, R. C.; Hofer-Warbinek, R.; Egelseer, E. M.; Sleytr, U. B.; Sara, M. A Functional Chimaeric S-Layer-Enhanced Green Fluorescent Protein to Follow the Uptake of S-Layer-Coated Liposomes into Eukaryotic Cells. *Biochem. J.* **2004**, *379*, 441–448.
12. Ilk, N.; Vollenkle, C.; Egelseer, E. M.; Breitwieser, A.; Sleytr, U. B.; Sara, M. Molecular Characterization of the S-Layer Gene, *sbpA*, of *Bacillus sphaericus* CCM 2177 and Production of a Functional S-Layer Fusion Protein with the Ability to Recrystallize in a Defined Orientation While Presenting the Fused Allergen. *Appl. Environ. Microbiol.* **2002**, *68*, 3251–3260.
13. Moll, D.; Huber, C.; Schlegel, B.; Pum, D.; Sleytr, U. B.; Sara, M. S-Layer-Streptavidin Fusion Proteins as Template for Nanopatterned Molecular Arrays. *Proc. Natl. Acad. Sci. U. S. A.* **2002**, *99*, 14646–14651.
14. Tschiggerl, H.; Breitwieser, A.; de Roo, G.; Verwoerd, T.; Schaffer, C.; Sleytr, U. B. Exploitation of the S-Layer Self-Assembly System for Site Directed Immobilization of Enzymes Demonstrated for an Extremophilic Laminarinase from *Pyrococcus furiosus*. *J. Biotechnol.* **2008**, *133*, 403–411.
15. Shenton, W.; Pum, D.; Sleytr, U. B.; Mann, S. Synthesis of Cadmium Sulphide Superlattices Using Self-Assembled Bacterial S-Layers. *Nature* **1997**, *389*, 585–587.
16. Pum, D.; Sleytr, U. B. Anisotropic Crystal Growth of the S-Layer of *Bacillus sphaericus* CCM 2177 at the Air/Water Interface. *Colloids Surf., A* **1995**, *102*, 99–104.
17. Korkmaz, N.; Ostermann, K.; Rodel, G. Calcium Dependent Formation of Tubular Assemblies by Recombinant S-Layer Proteins *In Vivo* and *In Vitro*. *Nanotechnology* **2011**, *22*, 095601.
18. Chung, S.; Shin, S. H.; Bertozzi, C. R.; De Yoreo, J. J. Self-Catalyzed Growth of S Layers *via* an Amorphous-to-Crystalline Transition Limited by Folding Kinetics. *Proc. Natl. Acad. Sci. U. S. A.* **2010**, *107*, 16536–16541.
19. Norville, J. E.; Kelly, D. F.; Knight, T. F., Jr.; Belcher, A. M.; Walz, T. 7Å Projection Map of the S-Layer Protein SbpA Obtained with Trehalose-Embedded Monolayer Crystals. *J. Struct. Biol.* **2007**, *160*, 313–323.
20. Teixeira, L. M.; Strickland, A.; Mark, S. S.; Bergkvist, M.; Sierra-Sastre, Y.; Batt, C. A. Entropically Driven Self-Assembly of *Lysinibacillus sphaericus* S-Layer Proteins Analyzed under Various Environmental Conditions. *Macromol. Biosci.* **2010**, *10*, 147–155.
21. Andreu, J. M.; Timasheff, S. N. The Measurement of Cooperative Protein Self-Assembly by Turbidity and Other Techniques. *Methods Enzymol.* **1986**, *130*, 47–59.
22. Hurshman, A. R.; White, J. T.; Powers, E. T.; Kelly, J. W. Transthyretin Aggregation under Partially Denaturing Conditions Is a Downhill Polymerization. *Biochemistry* **2004**, *43*, 7365–7381.
23. Baranova, E.; Fronzes, R.; Garcia-Pino, A.; Van Gerven, N.; Papapostolou, D.; Pehau-Arnaudet, G.; Pardon, E.; Steyaert, J.; Howorka, S.; Remaut, H. SbsB Structure and Lattice Reconstruction Unveil Ca^{2+} Triggered S-Layer Assembly. *Nature* **2012**, *487*, 119–122.
24. Shin, S. H.; Chung, S.; Sanii, B.; Comolli, L. R.; Bertozzi, C. R.; De Yoreo, J. J. Direct Observation of Kinetic Traps Associated with Structural Transformations Leading to Multiple Pathways of S-Layer Assembly. *Proc. Natl. Acad. Sci. U. S. A.* **2012**, *109*, 12968–12973.
25. Allen, K. N.; Imperiali, B. Lanthanide-Tagged Proteins—an Illuminating Partnership. *Curr. Opin. Chem. Biol.* **2010**, *14*, 247–254.
26. Selvin, P. R. Principles and Biophysical Applications of Lanthanide-Based Probes. *Annu. Rev. Biophys. Biomol. Struct.* **2002**, *31*, 275–302.
27. Eftink, M. R. Fluorescence Methods for Studying Equilibrium Macromolecule-Ligand Interactions. *Methods Enzymol.* **1997**, *278*, 221–257.
28. Thomä, N.; Goody, R. S. What to Do If There Is No Signal: Using Competition Experiments to Determine Binding Parameters. In *Kinetic Analysis of Macromolecules: A Practical Approach*; Johnson, K., Ed.; Oxford University Press: Oxford, U.K., 2003; pp 153—170.
29. Horejs, C.; Gollner, H.; Pum, D.; Sleytr, U. B.; Peterlik, H.; Jungbauer, A.; Tscheliessnig, R. Atomistic Structure of Monomolecular Surface Layer Self-Assemblies: Toward Functionalized Nanostructures. *ACS Nano* **2011**, *5*, 2288–2297.
30. Gasteiger, E.; Hoogland, C.; Gattiker, A.; Wilkins, M. R.; Appel, R. D.; Bairoch, A. Protein Identification and Analysis Tools on the Expasy Server. In *The Proteomics Protocols Handbook*; Springer: Berlin, 2005; pp 571—607.
31. Wong, G. C.; Pollack, L. Electrostatics of Strongly Charged Biological Polymers: Ion-Mediated Interactions and Self-Organization in Nucleic Acids and Proteins. *Annu. Rev. Phys. Chem.* **2010**, *61*, 171–189.
32. Sleytr, U. B.; Messner, P.; Pum, D.; Sara, M. Crystalline Bacterial Cell Surface Layers (S Layers): From Supramolecular Cell Structure to Biomimetics and Nanotechnology. *Angew. Chem.* **1999**, *38*, 1034–1054.

33. Dominguez, D. C. Calcium Signalling in Bacteria. *Mol. Microbiol.* **2004**, *54*, 291–297.

34. Norris, V.; Grant, S.; Freestone, P.; Canvin, J.; Sheikh, F. N.; Toth, I.; Trinei, M.; Modha, K.; Norman, R. I. Calcium Signalling in Bacteria. *J. Bacteriol.* **1996**, *178*, 3677–3682.

35. Knobel, L. L.; Bartholomay, R. C.; Cecil, L. D.; Tucker, B. J.; Wegner, S. J. *Chemical Constituents in the Dissolved and Suspended Fractions of Ground Water from Selected Sites, Idaho National Engineering Laboratory and Vicinity, Idaho, 1989*; U.S. Dept. of the Interior, U.S. Geological Survey: Washington, D.C., 1992; Books and Open-File Reports Section, Series 92−51, p 54.

36. Selzer, T.; Albeck, S.; Schreiber, G. Rational Design of Faster Associating and Tighter Binding Protein Complexes. *Nat. Struct. Biol.* **2000**, *7*, 537–541.

37. Zhang, F. J.; Zocher, G.; Sauter, A.; Stehle, T.; Schreiber, F. Novel Approach to Controlled Protein Crystallization through Ligandation of Yttrium Cations. *J. Appl. Crystallogr.* **2011**, *44*, 755–762.

38. Schuster, B.; Gyorvary, E.; Pum, D.; Sleytr, U. B. Nanotechnology with S-Layer Proteins. *Methods Mol. Biol.* **2005**, *300*, 101–123.

39. Gill, S. C.; von Hippel, P. H. Calculation of Protein Extinction Coefficients from Amino Acid Sequence Data. *Anal. Biochem.* **1989**, *182*, 319–326.

40. Shin, S. H.; Comolli, L. R.; Tscheliessnig, R.; Wang, C.; Nam, K. T.; Hexemer, A.; Siegerist, C. E.; De Yoreo, J. J.; Bertozzi, C. R. Self-Assembly of "S-Bilayers", a Step toward Expanding the Dimensionality of S-Layer Assemblies. *ACS Nano* **2013**, *7*, 4946–4953.

41. Schneider, C. A.; Rasband, W. S.; Eliceiri, K. W. NIH Image to ImageJ: 25 Years of Image Analysis. *Nat. Methods* **2012**, *9*, 671–675.

42. Voros, J. The Density and Refractive Index of Adsorbing Protein Layers. *Biophys. J.* **2004**, *87*, 553–561.

43. Querry, M. R.; Wieliczka, D. M.; Segelstein, D. J. Water (H_2O). In *Handbook of Optical Constants of Solids*; Edward, D. P., Ed.; Academic Press: Burlington, 1997; pp 1059−1077.

44. Hura, G. L.; Menon, A. L.; Hammel, M.; Rambo, R. P.; Poole, F. L., 2nd; Tsutakawa, S. E.; Jenney, F. E., Jr.; Classen, S.; Frankel, K. A.; Hopkins, R. C.; *et al.* Robust, High-Throughput Solution Structural Analyses by Small Angle X-Ray Scattering (SAXS). *Nat. Methods* **2009**, *6*, 606–612.

45. Konarev, P. V.; Volkov, V. V.; Sokolova, A. V.; Koch, M. H. J.; Svergun, D. I. Primus: A Windows PC-Based System for Small-Angle Scattering Data Analysis. *J. Appl. Crystallogr.* **2003**, *36*, 1277–1282.

46. Schiffer, R.; Thielheim, K. O. Light-Scattering by Dielectric Needles and Disks. *J. Appl. Phys.* **1979**, *50*, 2476–2483.

47. Ferri, J. K.; Stebe, K. J. Which Surfactants Reduce Surface Tension Faster? A Scaling Argument for Diffusion-Controlled Adsorption. *Adv. Colloid Interface Sci.* **2000**, *85*, 61–97.